Journal of
Materials Chemistry C

ROYAL SOCIETY OF CHEMISTRY

PAPER

View Article Online
View Journal | View Issue



Cite this: *J. Mater. Chem. C*, 2025, **13**, 21027

# A single-walled carbon nanotube-based phototransistor for neuromorphic vision applications

Jiahao Yao,[a] Jing Xu,[a] Hui Li,[a] Litao Sun,[a] Jianwen Zhao*[b] and Hongxuan Guo*[a]

With the continuous expansion of sensor networks, a vast amount of unstructured data is being generated, leading to frequent data transfers between sensors and computing units. This imposes significant challenges in terms of energy consumption, latency, storage, bandwidth, and data security. To address these issues, artificial synaptic devices have emerged as a research focus in neuromorphic hardware systems due to their suitability for novel parallel computing architectures, which offer higher efficiency and energy performance compared to the traditional von Neumann architecture when handling complex, large-scale information processing tasks. In this study, we present an inkjet-printed optoelectronic synaptic thin-film transistor (OSTFT) based on semiconducting single-walled carbon nanotubes (sc-SWCNTs), employing aluminum oxide ($Al_2O_3$) as the gate dielectric and a photoresponsive organic semiconductor material, $C_{74}H_{80}N_6S_4$ (OP064), as the light-sensitive layer. The device is capable of emulating key biological synaptic functions under both optical and electrical stimulation. A range of synaptic plasticity behaviors, including excitatory postsynaptic current (EPSC), inhibitory postsynaptic current (IPSC), paired-pulse facilitation (PPF), long-term potentiation (LTP), long-term depression (LTD), and spike-timing-dependent plasticity (STDP), have been systematically demonstrated. Furthermore, leveraging these synaptic functionalities, a spiking neural network (SNN) was constructed and validated through simulation for image classification on the MNIST dataset, exhibiting promising performance. This work highlights the potential of inkjet-printed sc-SWCNT-based OSTFTs incorporating OP064 as a photoresponsive medium in neuromorphic computing applications and provides a viable path toward high-efficiency, low-latency intelligent information processing systems.

Received 26th June 2025,
Accepted 2nd September 2025

DOI: 10.1039/d5tc02457a

rsc.li/materials-c

## 1 Introduction

In recent years, the number of nodes in sensor networks has exhibited a significant growth trend, and the data generated by these nodes are predominantly unstructured and highly redundant. Consequently, there is a frequent exchange of vast amounts of redundant information between sensor terminals and computing units. In traditional designs, due to differences in functional requirements and manufacturing techniques between sensing and computing, these components are typically physically separated. Sensor terminals locally acquire large volumes of raw data, which must then be transmitted to local computing units or cloud-based systems for processing. This data transmission mechanism has led to serious issues in terms of energy consumption, response latency, data storage, communication bandwidth, and security.[1] At this point, neuromorphic computing technology presents an attractive solution. The human brain is a highly parallel, energy-efficient, and low-power computing system. Inspired by the human brain, neuromorphic computing has gained increasing research interest and attention. In the nervous system, each neuron forms thousands of synaptic connections with other neurons, transmitting information *via* synapses. Currently, artificial synapses have been extensively studied and can generally be categorized into two-terminal and three-terminal devices. Two-terminal devices primarily implement artificial synaptic functions through memristors,[2–4] while three-terminal devices include electric double-layer transistors, optoelectronic transistors, and others.[5–9] Recent advancements in optogenetics and visual sensing technologies have gradually facilitated the incorporation of light into synaptic devices. Optoelectronic synaptic devices enable bidirectional conversion of optoelectronic signals, significantly advancing the

[a] *SEU-FEI Nano-Pico Center, Key Lab of MEMS of Ministry of Education, Southeast University, Nanjing, 210096, China. E-mail: ghx@seu.edu.cn*
[b] *Suzhou Institute of Nano-tech and Nano-bionics, Key Laboratory of Semiconductor Display Materials and Chips, Division of Nanodevices and Related Nanomaterials, Suzhou, 215123, China. E-mail: jwzhao2011@sinano.ac.cn*

development of optoelectronic artificial neural systems. Compared to traditional electronic synaptic devices, artificial optoelectronic synapses provide a non-contact operational method for neural systems, overcoming the limitations of electronic synapses.[10–12] Optoelectronic synaptic devices simulate the visual functions of biological synapses by adjusting synaptic weights, showing promise for the development of efficient brain-inspired computing systems. A commonly used approach involves employing optical pulses as presynaptic stimuli to induce continuous and reversible changes in conductivity, thereby enabling various neuromorphic computing characteristics.[13]

Printed electronics, benefiting from low-cost mass production, have gained significant attention.[14–16] Printed electronics is a novel additive manufacturing technology that employs printing processes and related techniques. Compared with traditional silicon-based technology, it offers advantages such as substrate independence, large-area scalable production, and environmentally friendly, low-cost fabrication. These benefits make it widely applicable for the preparation of electronic devices, including micro-electro-mechanical systems (MEMS), thin-film transistors, and sensors, and in recent years, it has also been applied in artificial synapse systems. Single-walled carbon nanotubes (SWCNTs) exhibit remarkable potential for thin-film transistors, attributed to their high carrier mobility and stable physical and chemical properties. As a promising semiconductor material in the post-Moore era, SWCNTs are gaining attention for their potential to revolutionize a variety of applications, including micro-nano sensing, integrated circuits, and other advanced technologies.[17,18]

In this study, an inkjet-printed optoelectronic synaptic thin-film transistor (OSTFT) based on sc-SWCNTs is demonstrated. The device employs aluminum oxide ($Al_2O_3$) as the gate dielectric and incorporates a photoresponsive organic semiconductor, $C_{74}H_{80}N_6S_4$ (OP064), which efficiently injects photogenerated carriers into the sc-SWCNT channel and modulates its electronic transport characteristics, thereby enhancing channel conductivity. Experimental results show that under electrical stimulation, gate-induced interfacial charges at the $Al_2O_3$/sc-SWCNT interface dynamically induce both synaptic potentiation and depression. Under optical stimulation, the device exhibits stable excitatory responses. The OSTFT demonstrates robust synaptic plasticity under both pure electrical and hybrid optical–electrical stimulation conditions. Key synaptic behaviors, including excitatory postsynaptic current (EPSC), inhibitory postsynaptic current (IPSC), paired-pulse facilitation (PPF), long-term potentiation (LTP), long-term depression (LTD), and spike-timing-dependent plasticity (STDP), are successfully emulated. Furthermore, capitalizing on the STDP characteristics of the device, a spiking neural network (SNN) was constructed using a biologically plausible STDP-based weight update algorithm.[19–21] The network was validated on a pattern recognition task using the modified National Institute of Standards and Technology (MNIST) handwritten digit dataset,[22] demonstrating the potential of the $Al_2O_3$-gated SWCNT-based OSTFT for neuromorphic visual recognition applications.

# 2 Experimental

## 2.1 Preparation of the PDMS encapsulation layer

Polydimethylsiloxane (PDMS) was used as an encapsulation layer to reduce the influence of ambient humidity during electrical measurements. The PDMS prepolymer, a viscous liquid, was extracted using a rubber-tipped dropper and transferred into a clean glass vial. A curing agent was added at a weight ratio of 10%, and the mixture was stirred magnetically for 10 minutes to ensure homogeneous blending. Since the mixture begins to solidify after the addition of the curing agent, it was prepared freshly prior to application. The resulting PDMS solution was spin-coated onto the device surface to form a thin, uniform isolation layer, effectively improving the stability and repeatability of synaptic performance measurements under varying environmental conditions. The spin-coating parameters were set as follows: rotation speed of 4000 rpm, spin time of 40 s, and immediate curing on a hot plate at 80 °C for 30 minutes after spin coating.

## 2.2 Preparation of sc-SWCNTS inks

To prepare the sc-SWCNT ink, 8.5 mg of SWCNT powder was mixed with 4.5 mg of an isoindigo-based poly(9,9-dioctylfluorene) derivative (PFIID) in 5 mL of toluene. The mixture was subjected to ultrasonication using a probe sonicator (Sonic & Materials Inc., Model: VCX 130, 85 W) at 0 °C for 45 minutes to achieve effective dispersion. Following sonication, the resulting suspension was sequentially centrifuged to remove undispersed nanotubes and aggregates: first at 1500 rpm for 1 hour, after which the supernatant was collected and further centrifuged at 2000 rpm for another hour. The final supernatant obtained after the two-step centrifugation process was used as the working sc-SWCNT ink solution.

## 2.3 Preparation of optoelectronic device

The fabrication of the inkjet-printed optoelectronic synaptic thin-film transistor based on sc-SWCNTs was accomplished through a streamlined, multilayer process optimized for compatibility with flexible substrates and solution-based techniques. Subsequently, a 15 nm $Al_2O_3$ gate dielectric was deposited *via* atomic layer deposition (ALD) at 120 °C, using trimethylaluminum and water as the respective metal and oxidant precursors. Source and drain electrodes composed of Ag were then patterned by aerosol jet printing and thermally dried to ensure film uniformity and electrical contact integrity. To promote strong interfacial adhesion between the semiconducting layer and the dielectric, the device was exposed to UV light irradiation for 1 minute. The semiconducting channel layer, consisting of sc-SWCNTs dispersed in a PFIID-based ink, was subsequently deposited by inkjet printing and thermally annealed at 120 °C for 3 minutes. Post-annealing treatment with toluene was employed to remove excess polymeric surfactant, followed by drying to finalize the nanotube network. Finally, a photoresponsive organic semiconductor, OP064, was spin-coated at a concentration of 1.5 mg $mL^{-1}$ and dried, forming the active photosensitive layer of the device.

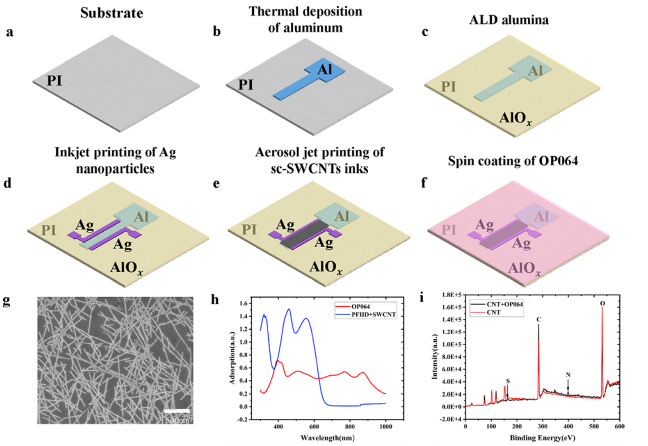


Fig. 1 Fabrication process of the PFIID-SWCNT-based TFT photosensitive device: (a) PI substrate preparation, (b) thermal deposition of the Al gate, (c) $Al_2O_3$ dielectric layer *via* ALD, (d) inkjet printing of Ag nanoparticles, (e) aerosol jet printing of sc-SWCNTs in the channel, and (f) spin-coating of OP064 photosensitive layer, (g) SEM image of SWCNTs, (h) adsorption spectra of the SWCNTs and OP064, and (i) the full XPS spectrum of carbon nanotubes and OP064.

The overall fabrication process is schematically illustrated in Fig. 1(a)–(f).

## 3 Results and discussion

Fig. 1(g) shows a scanning electron microscope (SEM) image of the sc-SWCNTs, displaying a dense and uniformly distributed network of carbon nanotubes with linear, fibrous structures. These nanotubes intertwine to form a net-like structure without any noticeable impurities or other extraneous structures. Fig. 1(h) presents the optical UV-Vis-NIR absorption spectrum of the sc-SWCNTs film and OP064, extending up to approximately 600 nm. In contrast to PFIID-SWCNT, the OP064 film

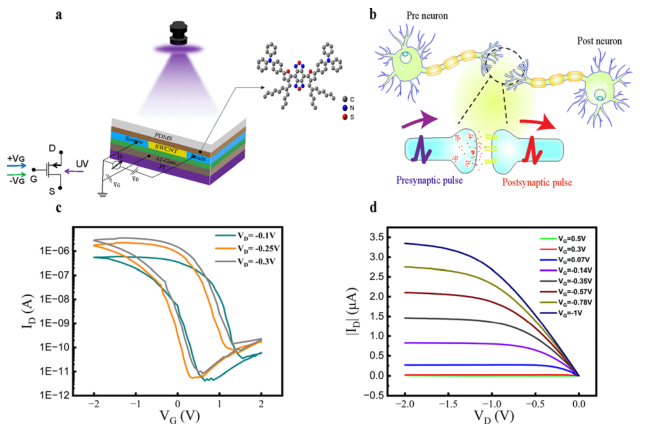


Fig. 2 (a) The structure and operating principle of the SWCNT-based thin-film transistor device. (b) A schematic of the synapse. (c) Transfer characteristic curve of drain current ($I_D$) *versus* gate voltage ($V_G$) at room temperature (300 K) with drain voltage $I_D$ = −0.1 V, $I_D$ = −0.25 V and $I_D$ = −0.3 V. (d) Output characteristic curve of drain current ($I_D$) *versus* drain–source voltage ($V_D$) at various gate–source voltages ($V_G$), ranging from −1 V to 0.5 V.

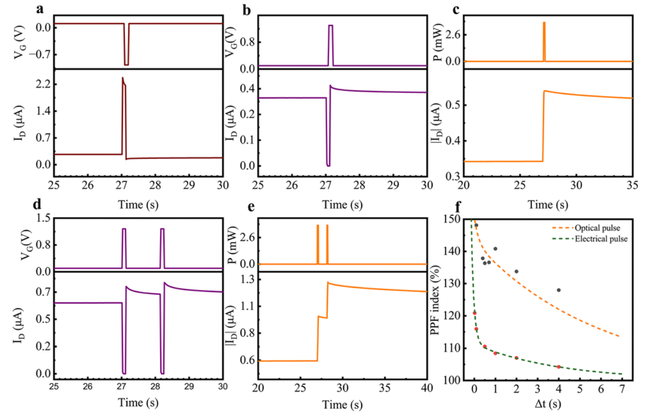


Fig. 3 Synaptic behavior and PPF characteristics of the device under electrical and optical pulses. (a) Current response of the device under negative gate voltage pulse, with an initial gate voltage of 0.1 V, a pulse voltage of −1 V, and a pulse width of 100 ms. (b) Current response of the device under positive gate voltage pulse, with an initial gate voltage of 0.1 V, a pulse voltage of 1.1 V, and a pulse width of 100 ms. (c) Current response of the device under optical pulse stimulation, with a light wavelength of 365 nm, a pulse width of 100 ms, and a power density of 3 mW $cm^{-2}$. (d) Current response of the device under paired positive pulses, with a pulse interval of 1 s. (e) Current response of the device under optical pulse stimulation with a pulse interval of 1 s. (f) PPF index as a function of the time interval (Δ*t*) for both optical and electrical spiking stimuli.

exhibits a broad absorption characteristic in the UV-Vis region, extending to around 900 nm. Consequently, the sc-SWCNTs film demonstrates the wavelength-dependent responsivity of the sc-SWCNTs-based optoelectronic synaptic transistor in both the UV and NIR regions. Fig. 1(i) displays the elemental analysis of the sc-SWCNTs thin film before and after the addition of OP064. Notably, the bounding energy exhibits prominent peaks at 165 eV and 400 eV, indicating the incorporation of sulfur (S) and nitrogen (N) elements on the surface of the carbon nanotube material. These findings confirm the successful coating of the carbon nanotube film with photosensitive material. The operating principle of the bioinspired synaptic device based on a sc-SWCNTs TFT is schematically illustrated in Fig. 2(a). Biological synapses, which serve as functional connectivity units between neurons, mediate the transmission of directional signals and the dynamic modulation of neural activity at their synaptic junctions. As depicted in Fig. 2(b), the presynaptic action potential triggered by suprathreshold stimulation induces the opening of voltage-gated ion channels in the presynaptic terminal, resulting in an ion influx. Localized elevation of ion concentration activates ion-sensitive proteins on synaptic vesicles, driving vesicle coupling and fusion with the presynaptic membrane to release neurotransmitters into the synaptic cleft. These neurotransmitters diffuse across the cleft and bind to specific postsynaptic receptors, inducing conformational changes in ion channels that regulate the excitability of the postsynaptic neuron. These synaptic behaviors can be emulated by applying electrical and optical pulses to the sc-SWCNT TFT and experimental characterization further confirms that the device exhibits synaptic plasticity. The device is capable of generating EPSCs and IPSCs on the basis of electrical signals, and it can produce EPSCs under optical stimulation. Fig. 2(c) shows the transfer characteristics of the device at room temperature (300 K), where a clear hysteresis is observed in the $I_{DS}$–$V_{GS}$ curve, indicating typical memory behavior. This effect is likely caused by charge trapping/detrapping at the channel/dielectric interface or trap states within the semiconductor. The hysteresis window is approximately 1 V and remains nearly independent of the drain voltage ($V_D$), suggesting stable electrical plasticity. Furthermore, the device exhibits a high on/off current ratio exceeding $10^5$, demonstrating strong gate modulation and favorable switching characteristics, which are essential for synaptic transistor applications in neuromorphic systems. Fig. 2(d) presents the output characteristic curve of the device, demonstrating its drain current as a function of the drain voltage ($V_D$) at different gate voltages. Fig. 3(a) presents the current behavior of the device under a single negative gate voltage pulse (−1 V, 100 ms). Following the application of the gate voltage, the synaptic current instantaneously decreases. After the pulse duration, the current increases to levels exceeding the initial value and gradually recovers over time. This delayed recovery after the increase in current is characteristic of EPSC. Fig. 3(b) illustrates the device's response to a positive gate voltage pulse (+1.1 V, 100 ms), where the synaptic current immediately increases, followed by a decline below the initial value after the pulse duration, subsequently recovering gradually over time, which is indicative of IPSC. Fig. 3(c) shows the enhanced synaptic current characteristic of EPSC under a single optical pulse (365 nm, 100 ms, 3 mW $cm^{-2}$), during the duration of the light pulse, the current increases instantaneously and continues to rise to a maximum value, gradually recovering after the duration of the pulse. Overall, the energy consumption per synaptic event across all stimulation modes (electrical and optical) is within the range of 30–270 nJ under the specified pulse intensities.

Synaptic plasticity refers to the property by which the strength of synaptic connections can be continuously adjusted, either strengthened or weakened in response to the activity level. Synaptic plasticity can be categorized into two types: LTP and STP. Short-term plasticity plays a crucial role in enabling short-term behaviors and is essential for short-term memory functions. PPF is a form of short-term synaptic plasticity, representing a neurological phenomenon where the postsynaptic potential increases when one stimulus closely follows another. Fig. 3(d) and (e) respectively illustrate the PPF characteristics of the synaptic phototransistor under two consecutive positive electrical pulses and two optical pulses. The interval between the pulses is 1 s, with each pulse having a duration of 100 ms, and the initial gate voltage before stimulation is set to 0.1 V. It is clearly observed that, under both electrical and optical stimulation, the second pulse elicits a higher postsynaptic current (PSC) than the first, indicating typical short-term synaptic enhancement behavior. This phenomenon strongly suggests the presence of significant charge trapping mechanisms within the device.[9] The cumulative effect of successive pulses leads to a progressive accumulation of electrons in these trap states, thereby inducing a form of plasticity analogous to LTP observed in biological synapses. Fig. 3(f) shows the correlation between the PPF ($PSC_2$/$PSC_1$) and

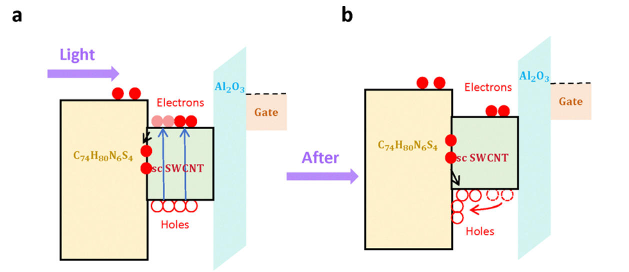


Fig. 4 Schematic illustration of the working mechanism under light stimulation in the p-type device. (a) Upon 365 nm UV illumination, the OP064 layer generates electron–hole pairs. Photogenerated electrons become trapped in the OP064 layer or at the interface, inducing a local negative electric field that facilitates hole accumulation in the p-type sc-SWCNT channel. (b) After illumination, the increased hole concentration persists temporarily, resulting in reduced channel resistance and enhanced conductance. This corresponds to excitatory synaptic behavior modulated by optical input.

the time interval ($\Delta t$). The PPF index is fitted by the equation $\mathrm{PPF} = 1 + A_1 \exp\left(\frac{-t}{t_1}\right) + A_2 \exp\left(\frac{-t}{t_2}\right)$, where the decay times are related to the decrease in the PPF index for both optical and electrical pulse stimulations. Under optical stimulation, the slow and fast decay times are $\tau_1$ = 0.2 ms and $\tau_2$ = 5.99 ms, respectively. Under electrical stimulation, the slow and fast decay times for positive electrical pulses are $\tau_1$ = 0.12 ms and $\tau_2$ = 4.05 ms, respectively. These decay time constants are comparable to the timescales of biological synapses, both exhibiting a fast decay phase and a slow decay phase. This indicates that the device can emulate some short-term plasticity characteristics of biological neurons, possessing a double-exponential decay characteristic. Through repeated pulse stimulation, short-term memory can be transformed into long-term memory. As shown in Fig. S1a, LTP is observed after the application of ten consecutive optical pulses at various wavelengths. The results indicate that wider optical pulses induce a greater enhancement in the postsynaptic current, demonstrating a strong dependence on pulse width. Fig. S1b–d present the frequency-dependent synaptic plasticity behaviors under different stimulation modes. Specifically, Fig. S1b and d illustrate the LTP effect induced by positive electrical pulses and optical pulse stimulation at varying frequencies, while Fig. S1c shows the LTD responses under negative electrical pulses. These results confirm that the device not only emulates short-term synaptic plasticity but also effectively achieves the transition to long-term synaptic modulation, highlighting its potential for neuromorphic computing applications. Moreover, the long-term memory effect of the optosensitive device can also be inferred from the data presented in Fig. S2. As shown in Fig. 4, the energy band diagram before and after illumination reveals the working mechanism of the device. Under 365 nm ultraviolet illumination, the OP064 photosensitive layer absorbs photons and generates electron–hole pairs. The photogenerated electrons become trapped in the OP064 layer or at the OP064/SWCNT interface, leading to the formation of a localized negative electric field. This field facilitates hole injection into

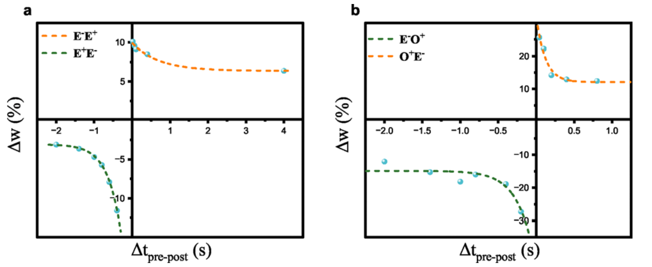


Fig. 5 The STDP characteristics of synaptic transistor: the $\Delta w$ depends on the time interval ($\Delta t_{pre\text{-}post}$) between the presynaptic and postsynaptic spikes in the combination of (a) $E^+E^-$ ($E^+$ represents a positive electrical pulse, and $E^-$ represents a negative electrical pulse), and (b) $O^+E^-$ ($O^+$ represents an optical pulse, and $E^-$ represents a negative electrical pulse).

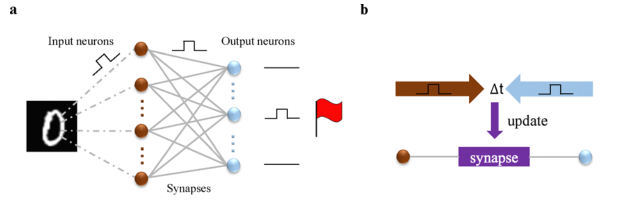


Fig. 6 (a) Schematic diagram of the spiking neural network (SNN) architecture used for handwritten digit recognition, and (b) schematic diagram of the STDP-based synaptic weight update strategy.

the p-type SWCNT channel, thereby increasing the hole concentration, reducing the channel resistance, and enhancing the conductance. Even after illumination ceases, this induced effect can persist for a certain duration, manifesting as a short-term enhancement in synaptic behavior. This mechanism accounts for the observed increase in channel conductivity and synaptic performance under optical stimulation.

Repeated and sustained stimulation can enhance the connectivity and information transmission between synapses, leading to tighter associations that facilitate LTP. STDP involves the dynamic modulation of synaptic strength, which is determined by the temporal difference ($\Delta t_{\text{pre-post}}$) between the firing of presynaptic and postsynaptic neurons. When the interval between two spikes is short, the magnitude of synaptic weight change becomes more pronounced. This mechanism can induce both LTP and LTD. Similar findings regarding spike-timing-dependent plasticity have been observed across various neural systems.[23–25] Typically, synapses are strengthened when a presynaptic spike occurs shortly before the postsynaptic neuron fires, but they are weakened if the spike order is reversed. However, in certain organisms, the opposite effect is observed. For instance, in the cerebellar structure of electric fish, presynaptic input arriving shortly before a postsynaptic spike leads to synaptic weakening.[26] This distinction classifies STDP into Hebbian and anti-Hebbian plasticity. Fig. 5 presents the results of our device's STDP experiments, showing that both purely electrical pulses and optoelectrical pulses align with anti-Hebbian plasticity. The following equation was used for fitting our experimental data:

$$\Delta W = A\exp\left(-\frac{\Delta t}{\tau}\right) + \Delta W_0 \quad (1)$$

Here, $\Delta W$ denotes the percentage change in synaptic weight, capturing how much the synaptic efficacy increases or decreases in response to spike-timing differences. $A$ and $\tau$ represent the scaling constant and time constant, respectively, which characterize the relative change in synaptic weight. Two correlated spikes with different waveforms and time intervals were applied to the device, with various waveform combinations implemented *via* optoelectronic and fully electronic methods. Fig. 5 shows the relationship between synaptic weight and the time difference $\Delta t_{\text{pre-post}}$ for the fully electronic system and the optoelectronic system, respectively. The initial gate voltage was set to 0.1 V, and the pulse parameters were the same as those described in previous sections. Fig. 5(a) illustrates the STDP measured in the fully electronic system, where the red dashed line indicates that synaptic weight increases when the negative pulse precedes the positive pulse ($\Delta t_{\text{pre-post}} > 0$). When $\Delta t_{\text{pre-post}}$ is less than 0, the synaptic weight decreases. Fig. 5(b) presents the STDP measured using the optoelectronic hybrid approach; when the negative electrical pulse precedes the optical pulse ($\Delta t_{\text{pre-post}} > 0$), the synaptic weight increases, and *vice versa*, the synaptic weight decreases. The specific measured STDP data and methods are shown in Fig. S3. From the measurement results, the device exhibits a unique dual-mode STDP characteristic, capable of achieving STDP by applying voltage at the gate as well as by applying optical signals to the photosensitive material. This dual-mode feature not only expands the application scenarios of the device but also opens new possibilities for future neuromorphic computing and multimodal sensing. When voltage is applied to the gate, the device's STDP characteristic enables synaptic weight updates to occur entirely through electronic processes. To investigate the device's capacity for unsupervised data processing in both modes, simulations were conducted to construct a SNN incorporating STDP-based synaptic weight update algorithms. A SNN based on the STDP device was created for a more complex task: recognizing handwritten digits from the MNIST database using an unsupervised SNN algorithm. Based on observed STDP-driven synaptic weight changes, the weight update rules for the SNN were defined as follows:

$$w_{\text{new}} = \begin{cases} w + \sigma\cdot\Delta W\cdot(w - |W_{\min}|)^{\mu} & \text{if } \Delta W < 0 \\ w + \sigma\cdot\Delta W\cdot(W_{\max} - w)^{\mu} & \text{if } \Delta W > 0 \end{cases} \quad (2)$$

The structure of the constructed spiking neural network (SNN) is illustrated in Fig. 6(a). Each pixel of a handwritten digit image is first converted into a spike sequence and delivered to the receiving layer, which consists of 784 neurons corresponding to the 28 × 28 image resolution. These neurons transmit information through synapses to the output layer, which contains 800 neurons. The output neurons are not assigned one-to-one to the 10 classification labels. Instead, a population coding strategy is employed, whereby the 800

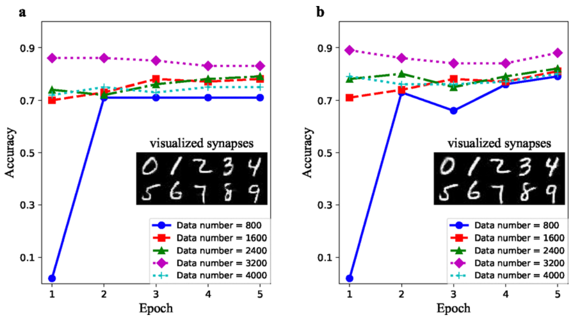

Fig. 7 Accuracy of the Spiking Neural Network trained using STDP. (a) Fully electric system performance over different epochs and dataset sizes (800, 1600, 2400, 3200, and 4000 samples), with an inset showing the corresponding visualized synapses; (b) optoelectronic system performance over the same conditions, with an inset for its visualized synapses.

neurons are evenly divided into 10 neuronal subgroups, each comprising 80 neurons and representing a specific class (digits 0–9). During training, neurons within the target class subgroup exhibit stronger spiking responses to input patterns belonging to their respective class, while non-target subgroups remain relatively inactive. During inference, the network determines the predicted class by analyzing the spiking activity—such as firing rate or total spike count—of each neuronal subgroup, and selects the class corresponding to the most active group.

Fig. 7(a) and (b) display the training results on different amounts of the MNIST dataset for the fully electronic and optoelectronic systems, respectively. Specifically, the training subsets consisted of 800, 1600, 2400, 3200, and 4000 images, which were randomly selected from the complete MNIST dataset of 60 000 images. The sampling was performed uniformly across all 10 digit classes, meaning that each subset contained approximately equal numbers of images for each class. This strategy ensured balanced class distribution and effectively avoided training bias. The results under different dataset sizes demonstrate that the network exhibits a high sensitivity in synaptic plasticity during the early stages of training. For example, when only 800 images were used, the network was nearly unable to perform classification after the first training epoch. In contrast, once the number of training images increased to 1600 in the second epoch, the classification accuracy improved significantly, and the synaptic structure became clearly optimized. When the training set size exceeded 1600 images, a single training epoch was generally sufficient to establish relatively effective synaptic connections, and further increases in training data led to only marginal improvements in accuracy. These observations indicate that the most significant enhancement in classification performance occurs when the network is stimulated by approximately 1600 images. Beyond this point, the contribution of additional training data becomes limited. It can be observed that with 3200 images, the training accuracy is highest, reaching 86% for the fully electronic system and 89% for the optoelectronic system. Unlike conventional BP neural networks, the STDP-based SNN adjusts synaptic weights through neurons' spontaneous activity and temporal dependencies, without relying on dataset labels, and thus cannot extract better features from an excessively large number of data samples. In Fig. 7(a) and (b), the insets display the synaptic weight maps after partial training for the fully electronic and optoelectronic systems, respectively. Comparing the visualized synapses of the two systems reveals that the optoelectronic system has sharper edges, which enhances the contrast between patterns and background, thereby improving recognition accuracy. This improvement is attributed to the smaller time decay constant, $\tau$, in the optoelectronic system, which provides more precise temporal dependence and facilitates learning of finer features. Compared with previous work, as shown in Table 1, our system exhibits a certain advantage in accuracy among hardware simulation-based models, though there remains a gap of approximately 9% compared to software-implemented systems. The accuracy on a more complex dataset, FashionMNIST,[27] where both the fully electronic system and the optoelectronic system maintain an accuracy of approximately 60%. Through simulation, it is demonstrated that both the optoelectronic and fully electronic modes are capable of enabling spiking neural networks to perform image recognition tasks.

# 4 Conclusions

In summary, we have developed an optoelectronic device based on single-walled carbon nanotubes that has been validated through experiments and simulations for its applicability in neuromorphic vision systems. This flexible device exhibits both optically and electrically adjustable plasticity, achieving paired-pulse enhancement indices of 148% for optical stimulation and 122% for electrical stimulation, which underscores its excellent synaptic plasticity. Moreover, its spike-timing-dependent plasticity (STDP) capabilities enable the implementation of fully electrical

Table 1 The performance on the MNIST dataset compared with other STDP-based SNNs

| Learning method | Implementation method | Performance (%) | Model |
|---|---|---|---|
| SNN + STDP | Software | 93.5 | Querlioz *et al.* (2013)[28] |
| SNN + STDP | Software | 95.0 | Diehl and Cook (2015)[29] |
| SNN + BP | Software | 98.5 | Ferré *et al.* (2018)[30] |
| SNN + BP | Software | 98.1 | Liu *et al.* (2021)[31] |
| SNN + STDP | Hardware simulation | 80 | Tian *et al.* (2018)[32] |
| SNN + STDP | Hardware simulation | 63.21 | Mu *et al.* (2021)[6] |
| SNN + STDP | Hardware simulation | 92.8 | Wang *et al.* (2022)[7] |
| SNN + STDP | Hardware simulation (fe) | 86.0 | This work |
| SNN + STDP | Hardware simulation (oe) | 89.0 | This work |

and optoelectronic hybrid spiking neural networks, facilitating image classification tasks with promising performance, as demonstrated by recognition accuracies of 89% and 86% in optical and electrical modes, respectively. The effectiveness of our approach has been confirmed, suggesting that it can be extended to other synaptic optoelectronic materials, thereby paving the way for new strategies in intelligent bio-inspired vision systems and neuromorphic engineering.

## Author contributions

Jiahao Yao was responsible for data curation, formal analysis, investigation, methodology, software development, and writing – original draft. Jing Xu contributed to investigation, methodology, and validation. Hui Li was involved in data curation, project administration, and visualization. Litao Sun, Hongxuan Guo, and Jianwen Zhao contributed to funding acquisition, conceptualization, project administration, supervision, and writing – review & editing.

## Conflicts of interest

The authors declare no conflicts of interest.

## Data availability

The data supporting this article have been included as part of the SI. See DOI: https://doi.org/10.1039/d5tc02457a.

Additional data may be available from the corresponding author upon reasonable request.

## Acknowledgements

The authors acknowledge financial support from the National Natural Science Foundation of China (grant no. 12274073, T2321002) and the Jiangsu Province Innovation Support Program (Soft Science Research) Special Fund under grant-BK20243020.

## References

1 F. Zhou and Y. Chai, *Nat. Electron.*, 2020, **3**, 664–671.
2 S. H. Jo, T. Chang, I. Ebong, B. B. Bhadviya, P. Mazumder and W. Lu, *Nano Lett.*, 2010, **10**, 1297–1301.
3 S. P. Adhikari, C. Yang, H. Kim and L. O. Chua, *IEEE Trans. Neural Netw. Learn. Syst.*, 2012, **23**, 1426–1435.
4 K. Chen, K. Pan, S. He, R. Liu, Z. Zhou, D. Zhu, Z. Liu, Z. He, H. Sun and M. Wang, *et al.*, *Adv. Sci.*, 2024, **11**, 2400966.
5 Q. Wu, B. Dang, C. Lu, G. Xu, G. Yang, J. Wang, X. Chuai, N. Lu, D. Geng, H. Wang and L. Li, *Nano Lett.*, 2020, **20**, 8015–8023.
6 B. Mu, L. Guo, J. Liao, P. Xie, G. Ding, Z. Lv, Y. Zhou, S.-T. Han and Y. Yan, *Small*, 2021, **17**, 2103837.
7 C. Wang, X. Xu, X. Pi, M. D. Butala, W. Huang, L. Yin, W. Peng, M. Ali, S. C. Bodepudi, X. Qiao, Y. Xu, W. Sun and D. Yang, *Nat. Commun.*, 2022, **13**, 5216.
8 D. Liu, J. Zhang, Q. Shi, T. Sun, Y. Xu, L. Li, L. Tian, L. Xiong, J. Zhang and J. Huang, *Adv. Mater.*, 2024, **36**, 2305370.
9 Y. Yoon, Y. Kim, S. Choi, J. Kwon and M. Shin, *Nano Res.*, 2024, **17**, 7631–7642.
10 X. Chen, B. Chen, B. Jiang, T. Gao, G. Shang, S.-T. Han, C.-C. Kuo, V. A. Roy and Y. Zhou, *Adv. Funct. Mater.*, 2023, **33**, 2208807.
11 Y. Wang, L. Yin, W. Huang, Y. Li, S. Huang, Y. Zhu, D. Yang and X. Pi, *Adv. Intell. Syst.*, 2021, **3**, 2000099.
12 N. Ilyas, J. Wang, C. Li, D. Li, H. Fu, D. Gu, X. Jiang, F. Liu, Y. Jiang and W. Li, *Adv. Funct. Mater.*, 2022, **32**, 2110976.
13 X. Zhu and W. D. Lu, *ACS Nano*, 2018, **12**, 1242–1249.
14 Z. Fan, J. C. Ho, T. Takahashi, R. Yerushalmi, K. Takei, A. C. Ford, Y.-L. Chueh and A. Javey, *Adv. Mater.*, 2009, **21**, 3730–3743.
15 T. Sekitani and T. Someya, *Adv. Mater.*, 2010, **22**, 2228–2246.
16 S. H. Kim, K. Hong, W. Xie, K. H. Lee, S. Zhang, T. P. Lodge and C. D. Frisbie, *Adv. Mater.*, 2013, **25**, 1822–1846.
17 L. Peng, Z. Zhang, S. Wang and X. Liang, *Sci. Sin. Tech.*, 2014, **44**, 1071–1086.
18 T. Sekitani, H. Nakajima, H. Maeda, T. Fukushima, T. Aida, K. Hata and T. Someya, *Nat. Mater.*, 2009, **8**, 494–499.
19 T. Iakymchuk, A. Rosado-Muñoz, J. F. Guerrero-Martínez, M. Bataller-Mompeán and J. V. Francés-Víllora, *EURASIP J. Image Video Process.*, 2015, **2015**, 4.
20 Y. Hao, X. Huang, M. Dong and B. Xu, *Neural Networks*, 2020, **121**, 387–395.
21 N. A. Rahman and N. Yusoff, *Neurocomputing*, 2025, **618**, 129170.
22 Y. Lecun, L. Bottou, Y. Bengio and P. Haffner, *Proceedings of the IEEE*, 1998, **86**, 2278–2324.
23 L. F. Abbott and S. B. Nelson, *Nat. Neurosci.*, 2000, **3**, 1178–1183.
24 G.-Q. Bi, *Biol. Cybern.*, 2002, **87**, 319–332.
25 N. Caporale and Y. Dan, *Annu. Rev. Neurosci.*, 2008, **31**, 25–46.
26 C. C. Bell, V. Z. Han, Y. Sugawara and K. Grant, *Nature*, 1997, **387**, 278–281.
27 H. Xiao, K. Rasul and R. Vollgraf, Fashion-MNIST: a Novel Image Dataset for Benchmarking Machine Learning Algorithms, *arXiv*, 2017, preprint, arXiv:1708.07747, DOI: 10.48550/rXiv:1708.07747.
28 D. Querlioz, O. Bichler, P. Dollfus and C. Gamrat, *IEEE Trans. Nanotechnol.*, 2013, **12**, 288–295.
29 P. U. Diehl and M. Cook, *Front. Comput. Neurosci*, 2015, **9**, 99.
30 P. Ferré, F. Mamalet and S. J. Thorpe, *Front. Comput. Neurosci*, 2018, **12**, 24.
31 F. Liu, W. Zhao, Y. Chen, Z. Wang, T. Yang and L. Jiang, *Front. Neurosci.*, 2021, **15**, 756876.
32 H. Tian, X. Wang, F. Wu, Y. Yang and T.-L. Ren, 2018 IEEE International Electron Devices Meeting (IEDM), 2018, pp. 38.6.1–38.6.4.